Subunit-specific conductance of single homomeric and heteromeric HCN pacemaker channels at femtosiemens resolution

Klaus Benndorf[a,1] ⓘD, Uta Enke[a] ⓘD, Debanjan Tewari[a] ⓘD, Jana Kusch[a] ⓘD, Haoran Liu[b,c] ⓘD, Han Sun[b,c] ⓘD, Ralf Schmauder[a] ⓘD, and Christian Sattler[a]

Affiliations are included on p. 10.

In mammals, the four subunit isoforms HCN1–4 assemble to form functional homotetrameric and heterotetrameric hyperpolarization-activated cyclic nucleotide-modulated (HCN) ion channels. Despite the outstanding relevance of HCN channels for organisms, including generating electrical rhythmicity in cardiac pacemaker cells and diverse types of brain neurons, key channel properties are still elusive. In particular, the unitary conductance, γ, of HCN channels is highly controversial. We analyzed the unitary conductance at femtosiemens resolution of all four homotetrameric channels of the mouse, mHCN1–4. All conductance values are in the range of 1 pS which is exceptionally small compared to most other ion channels. Surprisingly, the conductance among the isoforms differs up to threefold ($\gamma_{mHCN2} = 1.54$ pS $> \gamma_{mHCN1} = 0.84$ pS $> \gamma_{mHCN3} = 0.54$ pS $\approx \gamma_{mHCN4} = 0.51$ pS) though the residues in the two narrow parts of the pore, the selectivity filter and the inner gate, are conserved. Mutagenesis and all-atom molecular dynamics simulations demonstrate that the differences in the conductance are generated by different amounts of negative charges in the outer channel vestibule, which control ion accumulation. In line with these results, heterotetrameric channels exhibit intermediate unitary conductance values with respect to the homotetrameric channels. Our approach demonstrates how HCN channels can be functionally differentiated at the single-channel level, paving the way to target specific channels with selective drugs.

mHCN1–4 channels | single-channel conductance | negative charges in outer channel vestibule | heterotetramers | molecular dynamics simulations

Hyperpolarization-activated cyclic nucleotide-modulated (HCN) ion channels evoke the so-called "funny" current I_f (I_h, I_q) (1–3) that generates electrical rhythmicity in many types of neurons (4) and pacemaker cardiomyocytes (5). In neurons, these channels also contribute to the constraint of long-term potentiation, modulation of the working memory, synaptic transmission as well as resonance and oscillations (4).

The primary stimulus for the activation of HCN channels is hyperpolarization of the membrane voltage. The typically slow and sigmoid time course of activation of HCN channels opposes the repolarizing phase of the action potential and generates the slow depolarizing pacemaker potential (6). With sympathetic stimulation, the second messenger cAMP binds to the HCN channels, accelerating the electrical rhythmicity by enhancing channel activation.

In mammals, four subunit isoforms have been identified, HCN1–4 (2, 7, 8). All four subunit isoforms can form functional homotetrameric channels (9–11). Each subunit contains a cyclic-nucleotide binding domain (CNBD) in the C-terminus for the binding of cAMP (12), resulting in four CNBDs per channel. HCN2 (2) and HCN4 channels (13) are strongly stimulated by cAMP whereas HCN1 channels are reported to be less sensitive to cAMP (14). In contrast, for HCN3 channels no stimulating cAMP effect was found (11, 15). With heterologous expression, functional heterotetrameric channels have also been identified for HCN1/HCN2 (16, 17), HCN1/HCN4 (18), and HCN2/HCN4 (19). Heteromerization was confirmed for all combinations of isoforms by coimmunoprecipitation apart from HCN2/HCN3 (20). The channel architecture of homotetrameric HCN1, HCN3, and HCN4 channels has been elucidated by cryoelectron microscopy (cryo-EM), both in the presence and absence of bound cAMP (21–25).

The dual activation of HCN channels by voltage and cAMP has been widely studied in ensemble currents from HCN1, HCN2, and HCN4 channels, either in whole cells or macropatches containing typically hundreds of channels. Single-channel currents were

Significance

Hyperpolarization-activated cyclic nucleotide-modulated (HCN) ion channels control rhythmic electrical activities in the body, such as the heart beat and repetitive firing of brain neurons. The conductance of these channels, a basic channel feature, is highly controversial because it is viewed to be too small to get reliably measured or it is assumed to be unrealistically large. Here, we show at femtosiemens resolution that the unitary conductance of all four mammalian isoforms is extremely small and, by mutagenesis and molecular dynamic simulations, that it is isoform specific. Our approach opens insights into the clinically relevant class of HCN channels when trying to identify which HCN channel homo- or heteromer is expressed in different tissues, a prerequisite to develop tissue-specific drugs.

identified in sino-atrial pacemaker cells by DiFrancesco decades ago (1, 26), now known to be preferentially carried by the cardiac isoform HCN4 (27). Compared to the vast majority of ion channels, the conductance is exceptionally small, in the range of 1 pS. This makes their analysis technically very challenging. Among recombinant channels, only HCN2 channels have been analyzed at the single-channel level. Their conductance was determined to be ~1.5 pS (28) and 1.67 pS (29), confirming the low values for sino-atrial cells. Evidence for a similarly low conductance of 0.68 pS for HCN channels was also provided by nonstationary noise analysis in pyramidal neurons (30).

In contrast to these studies, larger conductance values by at least an order of magnitude were reported for HCN1, HCN2, and HCN4 channels (31, 32) and natural HCN channels in rat hippocampal neurons (33), however, without demonstrating the typical slow activation time course upon hyperpolarization. It is very unlikely that both the high and the low conductance values are true (34).

Given the controversy over the reported large and small conductance of HCN channels and the prominent roles of these HCN channels in heart and brain function, we performed systematic single-channel analyses of all four HCN isoforms of the mouse (mHCN) in patches of *Xenopus* oocytes expressing these channels heterologously. We demonstrate on the one hand that the single-channel conductance of all homomeric channels is small and aligns with the simulated conductance of mHCN2 channels based on atomistic molecular dynamic (MD) simulations. On the other hand, we found that the single-channel conductance differs significantly among the four isoforms, even though the amino acid sequence in the two narrow pore regions, the selectivity filter and the inner gate (21), is either identical or very similar across all isoforms.

By mutagenesis and MD simulations, we identified the molecular mechanism behind the differing unitary conductance, which is due to different amounts of negative charges in the outer vestibule of the channel pore, resulting in significant differences in the cation occupancy at the extracellular side. Last, we demonstrate at the single-channel level that mHCN2 subunits can form functional heteromers with each of the other three mHCN isoforms.

Results

Single-Channel Currents of the Four HCN Isoforms. In whole-oocyte recording with the TEVC technique, we observed that all four isoforms mHCN1–4 express robust currents (*SI Appendix,* Fig. S1*A*) and that both the voltage of half maximum steady-state activation and the slowness of activation follow the sequence mHCN3>mHCN4>mHCN2>mHCN1 (*SI Appendix,* Fig. S1 *B–D*). Together with the observed deactivation kinetics (*SI Appendix,* Fig. S1*E*) these data were used to set the conditions for single-channel recordings (Fig. 1) (*Materials and Methods* and *SI Appendix,* *Supplemental Results*).

As a reference, we first recorded unitary currents, *i*, from mHCN2 channels (Fig. 1*B*). To obtain a reasonable number of traces with no openings (nulls) for subtraction of leakage and capacitive currents, short pulses with respect to the full activation time were applied. Both the ensemble average currents (*Top*) and the idealized traces, reflecting the time course of the increasing open probability, $P_o(t)$, (*Bottom*) demonstrate the characteristic slow sigmodal activation. The amplitude of the unitary currents was locally measured from time intervals >50 ms before and after an opening transition to minimize effects of possible subtle changes of the leak.

The current amplitude was determined by amplitude histograms (*SI Appendix,* Fig. S2 *A and B*). Even the unitary tail currents at 50 fA at –30 mV were reliably resolved (*SI Appendix,*

Fig. S2*C*). Using Eq. **3**, a unitary conductance of $\gamma_{mHCN2} = 1.54 \pm 0.02$ pS was obtained (*SI Appendix,* Table S1). The scatter of the unitary conductance, illustrated by the box plot in Fig. 2*A* and the line in Fig. 2*B*, was computed by this value. Superimposition of the cumulative latency until the first opening, $cL_1(t)$, with $P_o(t)$ (Fig. 1 *B*, *Bottom*) reveals that $P_o(t)$ is mainly a function of $cL_1(t)$, indicating that the channels regularly remain open after they have once opened. These results not only confirm previous conductance values in the low range (28, 29) but also demonstrate that our recording conditions were well suited to reliably study unitary currents down to the range of 50 fA.

For mHCN1 channels, the more rapid activation and deactivation compared to mHCN2 allowed us to apply faster pulsing (Fig. 1*A*) while the remaining analysis was carried out analogously to that of the mHCN2 recordings. The illustrated traces at two voltages together with the ensemble average currents show again the characteristic sigmoidal activation time course (*Top*). Notably, the amplitude of the unitary currents was only about half as large as that for mHCN2 channels, resulting in a lower unitary conductance $\gamma_{mHCN1} = 0.84 \pm 0.01$ pS (Fig. 2 *A* and *B* and *SI Appendix,* Table S1). Superimposing $cL_1(t)$ with $P_o(t)$ (Fig. 1 *A*, *Bottom*) reveals that the activation time course is also mainly determined by $cL_1(t)$.

The single-channel analysis of the slowly activating mHCN3 and mHCN4 channels required longer hyperpolarizing pulses and intervals at the resting potential (c.f. *SI Appendix,* Fig. S1). Hence, both the pulses and the intervals at the resting potential were set to 4 s, resulting in a slow pulsing rate of 0.125 Hz. As an unfavorable consequence, the number of traces was much lower and too few nulls were available for subtraction. Therefore, single-channel idealization was performed from raw data by a semiautomated procedure (*Materials and Methods*). The amplitude of the currents was determined as described above.

Unitary mHCN3 currents often started after an exceptionally long first latency and regularly stayed open until the end of the hyperpolarizing pulse (Fig. 1*C*), yielding the single-channel conductance $\gamma_{mHCN3} = 0.54 \pm 0.01$ pS. This value is even smaller than that for mHCN1 channels (Fig. 2 *A* and *B* and *SI Appendix,* Table S1). A similar analysis was also performed for mHCN4 currents, as demonstrated for a 2-channel patch in Fig. 1*D*, yielding a single-channel conductance $\gamma_{mHCN4}=0.51 \pm 0.01$ pS, a value similar to that in mHCN3 channels (Fig. 2 *A* and *B* and *SI Appendix,* Table S1). For both mHCN3 and mHCN4 we also superimposed $cL_1(t)$ with $P_o(t)$ (Fig. 1 *C* and *D*, *Bottom*). The activation time courses are mainly determined by $cL_1(t)$, indicating that also these channels regularly stay open after they have once opened.

To test whether or not the exceptionally low conductance determined for mHCN4 channels is specific for the mouse, we investigated also the human isoform hHCN4 (*SI Appendix,* Fig. S3). All features, the sigmoidal averaged current time course, the matching superimposition of $P_o(t)$ with $cL_1(t)$ (*SI Appendix,* Fig. S3 *A*, *Bottom*) and the single-channel conductance $\gamma_{hHCN4} = 0.56 \pm 0.01$ pS (*SI Appendix,* Fig. S3 *B and C* and Table S1) resemble those in mHCN3 and mHCN4 channels. The minor difference $\gamma_{hHCN4} > \gamma_{mHCN4}$ is viewed to be second-tier and is not further interpreted. The difference in conductance to ~1pS (1, 26), published for endogenous pacemaker channels in sinoatrial cells [presumably HCN4 (27)], might be due to different ionic conditions.

To further substantiate that the single-channel currents reported herein are indeed from expressed mHCN channels, we applied the pertinent channel agonist cAMP (20 µM) to excised patches at single-channel resolution (*SI Appendix,* Fig. S4*A*), a saturating concentration for HCN2 and HCN4 channels (35, 36). Here, we used patches containing multiple channels, still with single-channel resolution, to minimize effects of stochastic openings, and we
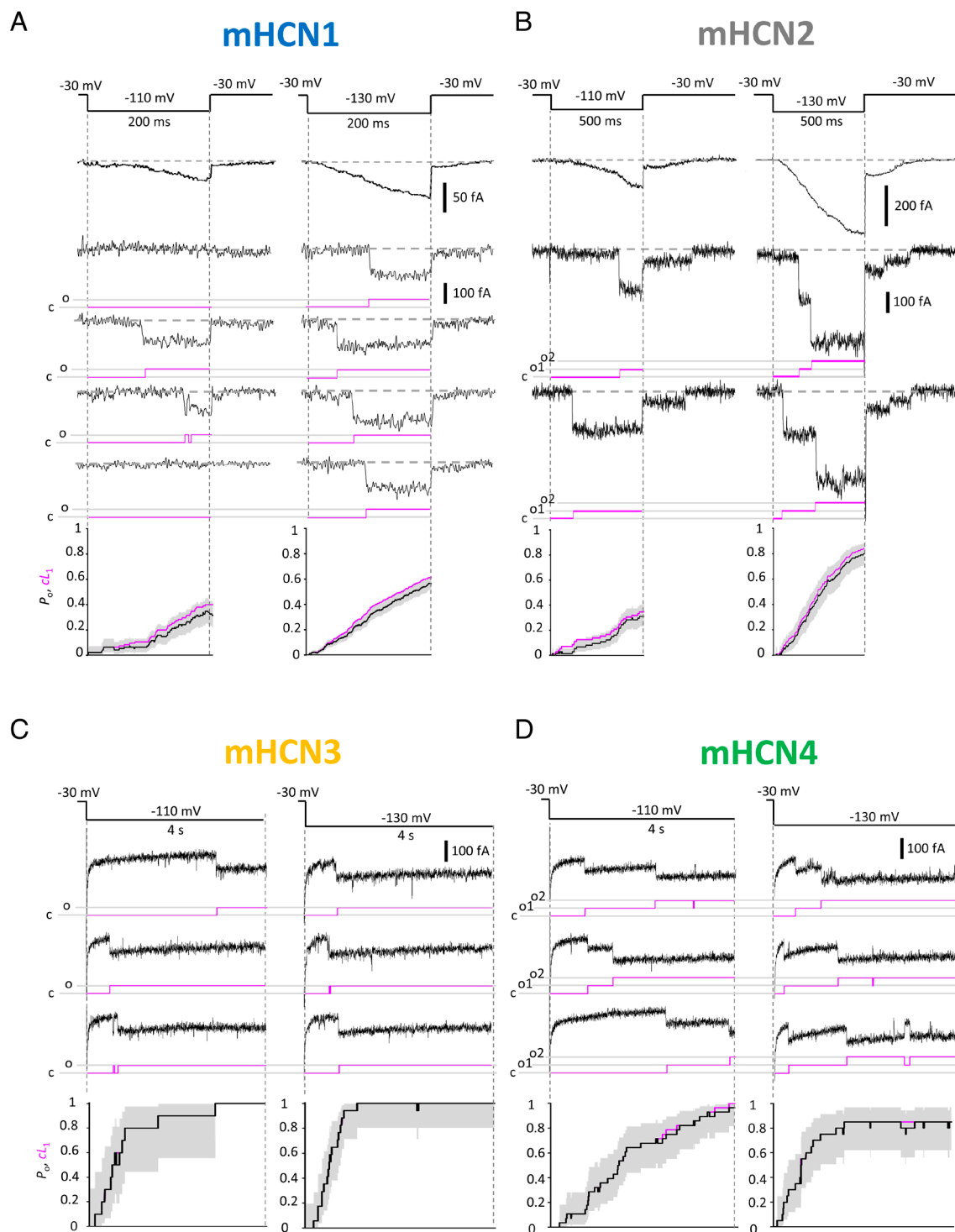
Fig. 1. Single-channel currents of wt mHCN channels. Representative traces and patches of the four indicated mHCN isoforms containing either one or two channels. The voltage was −110 and −130 mV. Below each trace, the corresponding idealized traces are shown in magenta; c: closed level; o or o1, o2: open level(s). *Bottom*: Superimposition of the cumulative first latency $cL_1(t)$ (magenta) with the open probability, $P_o(t)$ (black). The 95% CI along $P_o(t)$ are indicated in shades of gray. For all isoforms, $cL_1(t)$ approximately matches $P_o(t)$. (*A* and *B*) Fast activating mHCN1 and mHCN2 channels. Filter 200 Hz. The single-channel current traces were corrected for linear leakage and capacitive currents by subtracting nulls (mHCN1: −110 mV: 95 traces, 44 nulls; −130 mV: 371 traces, 108 nulls; mHCN2: −110 mV: 36 traces, 12 nulls; −130 mV: 58 traces, 1 null). The ensemble-average currents (*Top*) as well as the superimposed time courses of the idealized traces ($P_o(t)$) and cumulative first latency, $cL_1(t)$, (*Bottom*) were obtained from these corrected traces. (*C* and *D*) More slowly activating mHCN3 and mHCN4 channels. Filter 100 Hz. The traces were not corrected for linear leakage and capacitive components. For mHCN3, $P_o(t)$ and $cL_1(t)$ were formed from 10 (−110 mV) and 17 (−130 mV) traces whereas for mHCN4 14 (−110 mV) and 10 (−130 mV) traces were included. In case of mHCN3, $P_o(t)$ and $cL_1(t)$ superimpose nearly completely.

considered the activation time course. For all tested isoforms, mHCN1, mHCN3, and mHCN4, activation was notably accelerated (n = 4 for each isoform). The result was verified by three other experiments for each isoform. Among these effects that of mHCN1 is the smallest, confirming previous results (14). Because the ago-

nistic effect on mHCN3 conflicts with previous results (11, 15), we also measured steady-state activation in the absence and presence of 20 μM cAMP. Although the currents were very small, we observed a robust shift of activation to positive voltages. Moreover, we confirmed the accelerated activation by fitting an exponential yielding
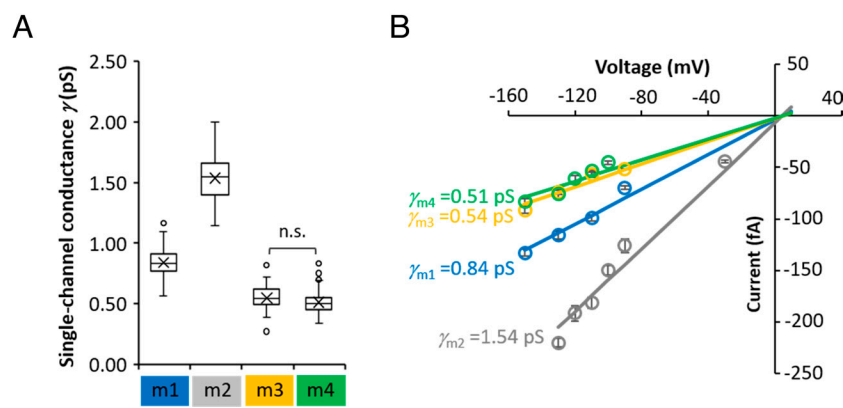
Fig. 2. Single-channel conductance of mHCN isoforms. (*A*) Boxplot of the unitary conductances. Outliers are included. The plot was generated from individual conductance values obtained by Eq. **3**, taking into account the reversal potential for the used K^+ concentrations (*Materials and Methods*). With $P = 0.01$ all conductance values are significantly different apart those for mHCN3 and mHCN4 (n.s.; pairwise *t* tests with Bonferroni–Holm correction). The numbers of included openings, n_{op}, and patches, n_p, are provided by *SI Appendix*, Table S1. (*B*) *iV*-relationships for unitary mHCN currents. The mean conductance values were used for calculating the straight lines. The conductance of the channels groups in the sequence $\gamma_{mHCN2} > \gamma_{mHCN1} > \gamma_{hHCN3} \approx \gamma_{hHCN4}$.

the time constant τ_{act} (*SI Appendix*, Fig. S5 *A* and *B*). Together with the previous results on mHCN2 channels (28, 29), our results demonstrate that cAMP up-regulates all four mHCN1–4 channels leaving the amplitude of the single-channel current unaffected (*SI Appendix*, Fig. S4*B*).

Molecular Mechanism for the Different Single-Channel Conductance of HCN Channels. We next addressed the question why the conductance of the HCN channels differs up to threefold. Alignment of the sequences (Fig. 3*A*) reveals that for all isoforms,

the two narrow pore regions (21), the selectivity filter (SF, CIGYG, green) and the inner gate (I(V)...T...Q, cyan), are conserved. This makes it unlikely that the conductance is defined simply by Ohm's law. We therefore performed mutagenesis in the wider pore region. Its amino-acid identity lies between 83 and 92%. All results are provided by the boxplot in Fig. 3*B* and *SI Appendix*, Table S2. To improve readability, mHCN1–mHCN4 will be abbreviated in the following by m1-m4.

Inserting the whole m2 pore into m4 (m4_Pore_m2) generates the large conductance typical for m2, indicating that the larger
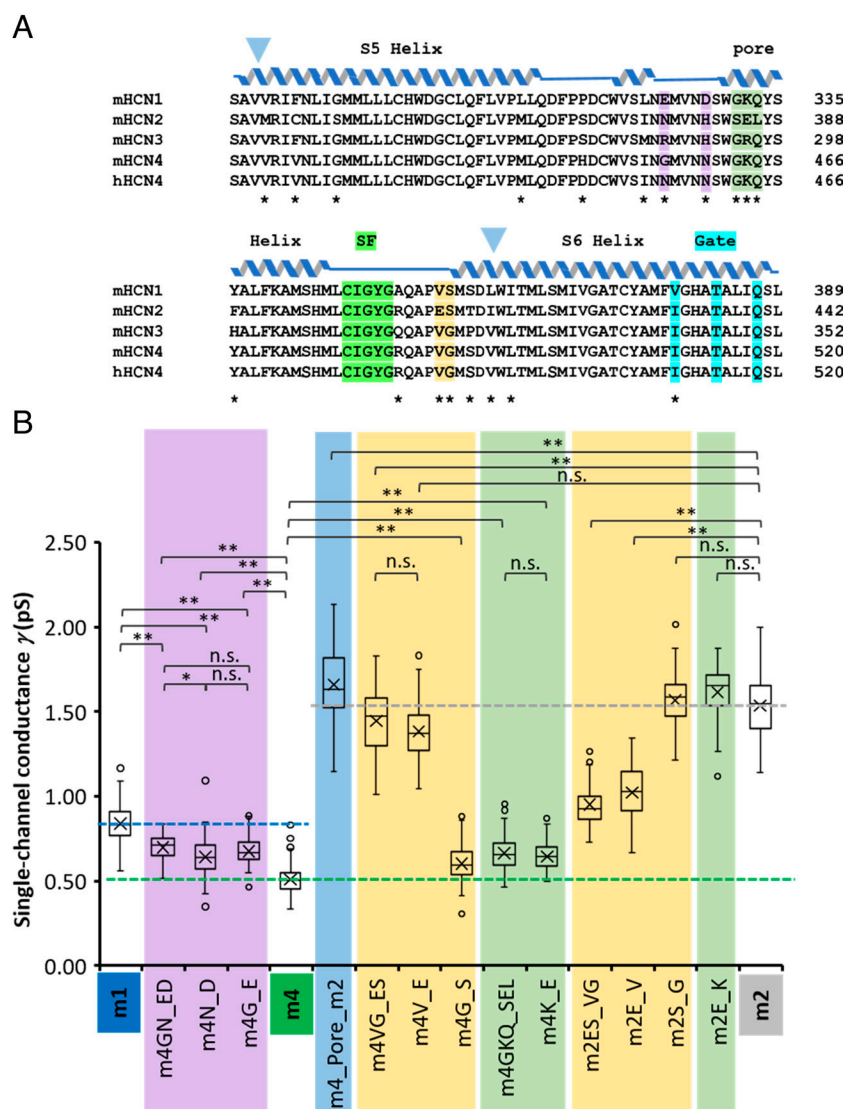
Fig. 3. Mutagenesis of key motifs in the pore region. To elucidate why the mHCN channels differ in their conductance by a factor of 3, conspicuous regions in the channel pore were mutated (see also *SI Appendix*, Table S2). (*A*) Sequence alignment of the pore regions for the four mouse isoforms and the human hHCN4. Green, selectivity filter (SF); cyan, inner gate. The three motifs differentiating the channels, m4GKQ_m2SEL (brown), m4VG_m2ES (olive), and m4G...N _ m1E...D (violet) were mutated. For m4_Pore_m2 the light blue triangles indicate the borders for differences in the pore between m2 and m4. (*B*) Boxplot of the unitary conductance of the mutants and relation to the wt channels. The colored dashed lines for the conductance of the wt channels serve as reference. Outliers are included. As in Fig. 2*A*, the conductance values were calculated from the individual conductance values. Relevant comparisons of the conductance values are indicated by parentheses. ** and * indicate a significant difference with $P < 0.01$ and $P < 0.05$, respectively, whereas n.s. means not significantly different (pairwise *t* tests with Bonferroni–Holm correction).

conductance is essentially generated by the pore region. The fact that the conductance is even slightly larger than that of m2 suggests an additional small current component by the channel background outside the pore region. It will not be further discussed herein.

We next considered differences between m2 and m4 within the pore region near the SF and the inner gate. Two motifs stand out immediately. In m4, proximal and distal to the SF, a GKQ and VG motif is substituted by a SEL and ES motif in m2, respectively, introducing two negatively charged glutamic acids.

We first transferred the whole ES motif of m2 into m4 and then both amino acids alone (m4VG_ES, m4V_E, m4G_S). The result is that the transfer of a negative glutamate alone generates a large conductance similar to that in m2. Hence, inserting a negative charge in the outer vestibule of the channel (c.f. Fig. 4 A and B) essentially augments the conductance. Transferring the second conspicuous m2 motif, SEL, to the respective GKQ position in m4 (m4GKQ_SEL) also augmented the conductance, but to a lesser extent. Transferring the glutamate alone caused an equal effect (m4K_E). To consolidate these effects of the two glutamates, we tested also several reverse m2 mutants where the respective m4

motifs were inserted (m2ES_VG, m2E_V, m2S_G, m2E_K). As expected, m2ES_VG and m2E_V reduced the conductance notably. The fact that the conductance is still somewhat larger than that of m4 suggests that here the still-present SEL motif plays a relevant role. As expected from this reasoning, m2S_G and m2E_K produced a conductance similar to m2. The results so far support the notion that negative charges in the external channel vestibule are responsible for the different conductance values of m2 and m4.

In the light of this, we finally considered the intermediate conductance of m1, a channel carrying the same GKQ and VG motif as m4. A conspicuous difference is two negative charges proximal to the GKQ motif (Fig. 3A). Transferring these charges to the corresponding positions in m4 either singly (m4N_D, m4G_E) or in combination (m4GN_ED) augmented the conductance in the direction to m1 without reaching it fully, indicating that in m1 channels an additional component must contribute to the larger conductance. The conclusion of these mutagenesis experiments is that the absence or presence of four negative residues in the channel vestibule strongly influences the specific conductance
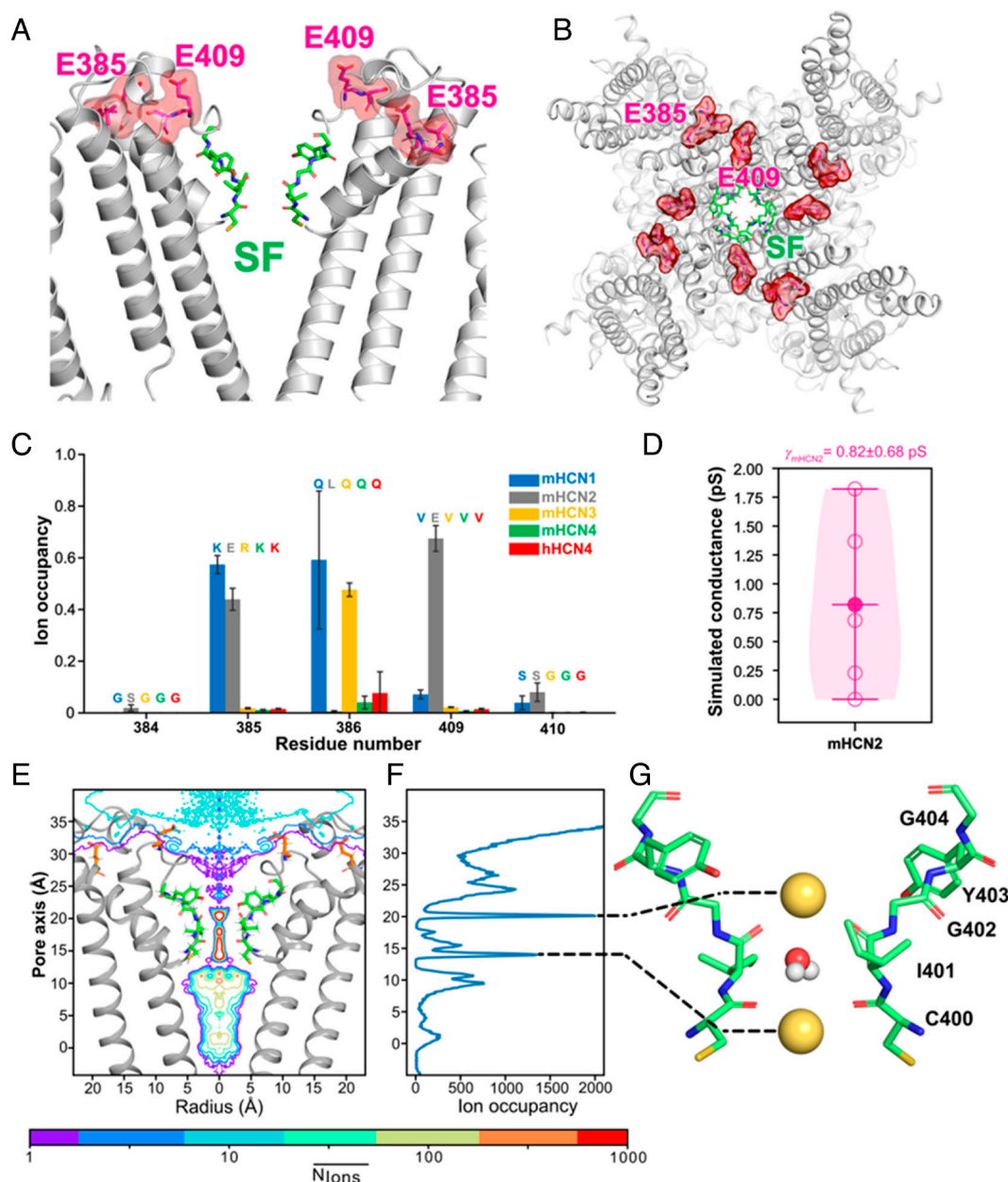
Fig. 4. MD simulations of HCN channels. (A) Side view and (B) top view of the mHCN2 channel with two key glutamic acid residues highlighted in red and SF residues shown in green. (C) Residue-wise K$^+$ occupancy of the SEL(GKQ,GRK) and ES(VS,VG) motifs derived from the simulations of mHCN1–4 and hHCN4 channels, respectively. Ion occupancy was calculated as the percentage of time the ion is in close proximity (within the first hydration shell of K$^+$: 3.4 Å). Three runs of 200 ns without transmembrane potential were performed for each channel. (D) Conductance derived from simulations of mHCN2, with circles representing the conductance from single simulation runs and the dot representing the average conductance from five parallel simulation runs. Each simulation was performed for 1 µs. (E) Two-dimensional absolute ion occupancy resolved radially and along the pore axis (z-axis) as a contour plot calculated from five runs of ion permeation simulations when applying a voltage of −700 mV. The orange residues are E385 and E409 as in A. (F) One-dimensional ion occupancy along the pore axis (z-axis) calculated from five runs of ion permeation simulations at −700 mV. (G) Snapshot of the mHCN2 SF showing the main populated K$^+$ ion configuration and water molecule within the SF.

of each HCN channel isoform. Among these residues, the glutamate in the ES motif of mHCN2 has the strongest effect.

Differences in Ion Occupancy of mHCN1–4 in the Outer Channel Vestibule Revealed by MD Simulations. To mechanistically understand the experimental findings, we conducted atomistic MD simulations on mHCN1–4 and hHCN4 channels. Homology structures of mHCN1–4 and hHCN4 were generated using the open conformation of the rabbit HCN4 channel (PDB ID: 7NP3) (23) as template. In this section, the numbering of mHCN2 channels is generally used. As shown in Fig. 4 *A* and *B*, two key glutamic acid residues in the SEL and ES motif identified as responsible for the larger single-channel conductance in the mHCN2 isoform, are located at the outer channel vestibule, with E409 in the ES motif of mHCN2 being closer to the ion conduction pathway.

We first performed MD simulations of mHCN1–4 channels without transmembrane voltage. These simulations revealed distinct residue-wise K^+ occupancy differences in the SEL(GKQ,GRQ) and ES(VS,VG) motifs between HCN1–4 (Fig. 4*C*), while the ion occupancy in the rest of the channels remained highly similar. Notably, E409 in mHCN2 showed a very high residue-wise K^+ occupancy, which was absent at this position in all other HCN isoforms. This finding aligns well with the experimental single-channel data, showing that mHCN2 exhibits the largest single-channel conductance among all HCN isoforms and that introducing a negatively charged glutamic acid residue in the ES motif into mHCN4 substantially increased its conductance.

We also compared the ion occupancy in the SEL(GKQ,GRQ) motif among different HCN isoforms. Here, the mHCN2 channel showed high K^+ occupancy at residue E385, while HCN1 exhibited high occupancy at the corresponding glycine and, most surprisingly, the neighboring lysine residue (Fig. 4*C*). Analysis of MD snapshots revealed that K^+ has a transient ion binding site close to these two residues, enabled by two negatively charged residues, E324 and D328 (*SI Appendix*, Fig. S6), that are spatially close to the K332 and adjacent to the SF. These results are again in excellent agreement with the recorded single-channel data, showing that introducing these two negatively charged residues into mHCN4 increased its conductance to match that of mHCN1. In conclusion, the comparison of single-channel data of mHCN1-mHCN4 with atomistic MD simulations confirmed the essential role of ion occupancy differences at the outer channel vestibule in explaining the single-channel conductance differences among the four HCN isoforms.

Since mHCN2 experimentally exhibits the largest single-channel conductance among the four isoforms, we simulated ion permeation through the mHCN2 channel by imposing negative transmembrane voltages during the simulations (37) https://zenodo.org/records/14278606. The simulated inward conductance of mHCN2 is 0.82 ± 0.68 pS (Fig. 4*D*), slightly lower than the experimental single-channel conductance of $\gamma_{mHCN2} = 1.54 \pm 0.02$ pS. Nonetheless, the simulated conductance of mHCN2 suggested a very low conductance value for the HCN channels, consistent with previously simulated low conductance values of rabbit HCN4 (38) and human HCN1 channels (25, 39). Analysis of one- and two-dimensional ion occupancy of mHCN2 channel along the ion permeation indicated substantial K^+ occupancy in the outer channel vestibule, partly contributed by the negatively charged E409 pointing toward the ion permeation pathway (Fig. 4 *E* and *F*). Furthermore, we observed distinct K^+ binding sites in the SF that are separated by a water molecule (Fig. 4*G* and *SI Appendix*, Fig. S7). This configuration closely resembles the SF ion occupancy profiles of a previously simulated rabbit HCN4 channel (38) but contrasts sharply with the K^+ permeation profile in the

SF of typical K^+ channels, where four consecutive ion-binding sites are almost equally populated by K^+ (40, 41).

mHCN2 Subunits Form Heteromeric Channels with All Three Other Isoforms. The specific conductance of the mHCN subunits provides a unique opportunity to study heteromerization at the single-channel level because a heteromer with different amounts of negative charges in the vestibule should generate different local concentrations of ions moving to the SF. In principle, when coexpressing two types of subunits (A and B) capable to heteromerize, they can form two homotetramers (AAAA, BBBB) and three heterotetramers [AAAB, AABB (cis and trans together), ABBB]. This would mean that three additional conductance values might appear between those of the homomers. To maximize resolution, we here tested the heteromerization capability of mHCN2 subunits with the other subunits because of its outstanding large conductance. Indeed, sublevels between the homotetramer conductances were observed for all investigated combinations (Fig. 5).

These experiments were performed at the voltage of –130 mV only (Fig. 5) and only patches were further analyzed that showed significant levels between those of the respective two wt channels. To best visualize the amplitudes of the single-channel currents of the heteromers between those of the homomers statistically, we preferred cumulative plots of the probability of a single-channel current to be larger than *x* fA, $P_{i>xfA}$ (Fig. 5 *A–C, Middle*) (For statistics, see *SI Appendix*, Table S3). For the wt channels, these $P_{i>xfA}$ plots generate steep relationships with clear separation apart from m3 and m4 (*SI Appendix*, Fig. S8). The slopes represent variability and resolution of our amplitude measurements.

Coexpressing m2 and m1 in a 1:2 RNA ratio showed that most of the openings were dominated by m1 while a minority generated either intermediate or m2 current levels (Fig. 5*A*). When increasing the RNA ratio to m2:m1 = 4:1, clearly more intermediate levels appeared and also m2 levels were more frequent. Coexpression of m2 and m3 in a 1:10 RNA ratio generated a $P_{i>xfA}$ relationship dominated by m2 though 10 times more m3 RNA was injected (Fig. 5*B*). We therefore injected first m3 RNA (day 0) and later (day 6) m2 RNA in a ratio 1:1. Current recordings, performed at day 7, yielded a significant portion of levels between both wt channels, demonstrating that also m3 subunits can heteromerize with m2 subunits. Coexpressing m2 and m4 in a 1:1 RNA ratio generated a $P_{i>xfA}$ relationship that was dominated by m2 but also containing a component between the two wt channels (Fig. 5*C*). When changing the RNA ratio to m2:m4=1:10, the $P_{i>xfA}$ relationship shifts to smaller current levels and significantly superimposes with m4, suggesting that the portion of m4 subunits in the heteromers has increased.

To test whether the intermediate unitary currents between those of the wt channels group to distinguishable levels (peaks), eventually reflecting different stoichiometries, we built histograms for the heteromeric combinations (Fig. 5, *Bottom*). The histograms for m2/m4 and m2/m3 indeed reveal discrete peaks, suggesting that an intermediate peak at larger current amplitude is generated by a heteromer with a higher number of m2 subunits due to more external charges in the m2 vestibule. One should be aware, however, that the amplitude of the peaks cannot be interpreted because the incidence of a current level depends also on the expression level of the subunits in a patch and the chance which channel constellation is included. For m2/m1, where the resolution is a priori inferior because of the smaller current difference between m2 and m1, distinct levels could not be identified unequivocally (Fig. 5 *A, Bottom*).
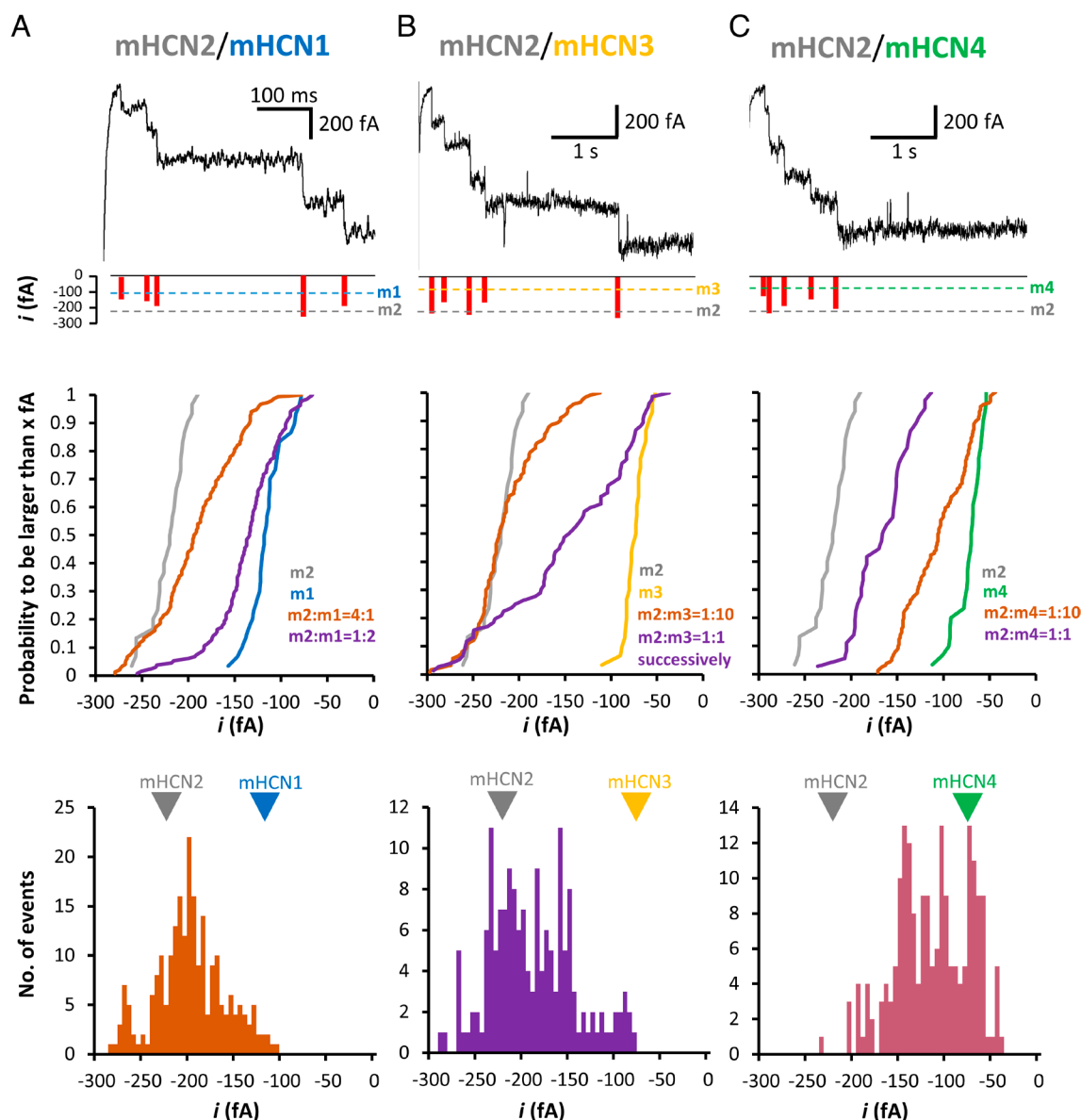
Fig. 5. Coexpression of mHCN2 subunits with all other HCN subunits. Different RNA mixtures were generated and injected. The mixtures are specified by ratios of the RNA mass. The voltage was generally −130 mV. On the *Top*, a representative trace of a multichannel patch is shown together with the amplitudes of the individual openings (red bars) determined by amplitude histograms. In the *Middle*, cumulative plots are illustrated for the probability of a single-channel current to be larger than *x* fA, $P_{i>xfA}$. At the *Bottom*, the incidence of current levels is plotted as function of the unitary current amplitude. Statistics are provided by *SI Appendix*, Table S3. (*A*) Coexpression of m2 and m1. At an RNA ratio m2:m1 = 1:2, most of the openings were dominated by m1 and while a minority of openings caused either an intermediate or the m2 current level. At an RNA ratio m2:m1 = 4:1, more intermediate and m2 levels became prominent. The bottom histogram includes 232 events from 60 traces with six channels of a single patch to avoid effects of patch variability. (*B*) Coexpression of m2 and m3. At m2:m3 = 1:10 still leaves m2 as dominating subunit. Subsequent RNA injection, m3 at day 0 and m2 at day 6 to 8 (ratio 1:1), resulted in a significant portion of levels between both wt channels. The bottom histogram includes 162 events from 59 traces of a single patch with ~12 channels to avoid effects of patch variability. (*C*) Coexpression of m2 and m4. At m2:m4 = 1:1 the relationship approximates m2 whereas at m2:m4 = 1:10 it is closer to m4. The bottom histogram was formed from all 197 events included in the cumulative plot.

Discussion

We showed that all four cloned mouse HCN channel isoforms, functionally identified by the characteristic slow and sigmoidal activation time course, generate a single-channel conductance in the order of 1 pS. Moreover, this single-channel conductance differs up to threefold in the sequence $\gamma_{mHCN2} > \gamma_{mHCN1} > \gamma_{mHCN3}, \gamma_{mHCN4}, \gamma_{hHCN4}$. These tiny conductance values are in good agreement with results on previous single-channel recordings in both native channels in cardiac sinus node cells (1, 26) and heterologously expressed mHCN2 channels (29, 42). They also confirm values obtained by nonstationary noise analysis in pyramidal neurons (30). The simulated conductance of mHCN2 by atomistic MD simulations on

the microsecond time scale is also in the order of 1 pS, aligning with the experimental single-channel conductance.

Because the amino acid sequence in the two narrow parts of the pore, the selectivity filter (CIGYG) and the inner gate (I(V)...T...Q), is conserved (Fig. 3*A*) (21), the conductance difference must arise from regions outside these narrow pore parts. We identified possible key players and verified them by mutagenesis (Fig. 3*B* and *SI Appendix*, Table S2). The key players for the larger conductance in the mHCN2 channel compared to the other isoforms are two negatively charged glutamic acids in the outer channel vestibule. In the sequence, one of these negatively charged residues is positioned proximal (SEL motif) and the other distal (ES motif) to the SF (Fig. 4 *A* and *B*). Notably, we observed excellent agreement

between the ion occupancy difference in these two motifs identified by MD simulations and the single-channel conductance, further confirming the essential role of the cation occupancy in the outer vestibule in modulating single-channel conductance of HCN channels. In mHCN1, generating about 60% larger conductance than mHCN4, two further negative charges were identified, also proximal to the SF, enhancing the ion occupancy at the GKQ motif (corresponding to the SEL motif in mHCN2).

The functional role of rings of negative charges in the channel vestibule to increase the single-channel conductance was extensively studied previously in structurally related voltage-gated sodium channels, generating an inward current of monovalent Na^+ ions (43–45). A proposed role of these charges is to concentrate Na^+ ions in the vestibule without binding them, supporting a knock-on mechanism for ion permeation (45). A similar effect of charges in the channel vestibule on K^+ ions is likely for HCN channels.

Our coexpression experiments of mHCN2 with either of the other subunits could clearly induce conductance values in between those of the homomeric channels using different RNA ratios to approximately cover the range between the respective wt channels (Fig. 5, *Middle*). The extreme case was m2/m3. Even in a 1:10 ratio the unitary currents were by far dominated by m2, which again fits to the exceptionally long incubation times of 7-13 days required for m3 alone. To prove the principal capability of the m3 subunits to form heteromers with m2, we used successive RNA injection in a 1:1 ratio (day 0 m3, day 6 to 8 m2; measurement within 24 h after m2 injection) and obtained intermediate unitary currents. Though it remains to be shown if such a scenario can appear in nature, it shows that the two types of subunits can assemble. Mechanistically, it is assumed that m3 subunits are produced slowly and linger in the endoplasmic reticulum as monomers or incomplete channels, perhaps in complexes with chaperones (46). After injection of the m2 RNA, the robust expression of m2 subunits leads to an assembly with the already present m3 subunits.

The pronounced peaks of the intermediate current levels (Fig. 5, *Bottom*) might reflect at least for m2/m4 and m2/m3 channels different stoichiometries (or geometries) of the subunits. This supports the notion that m2 subunits with the identified two negative charges in the SEL and ES motif contribute to the overall conductance in a graded manner depending on the number of subunits included in the channel. Nevertheless, from our present data, it is too early to unequivocally assign the current peaks to the subunit composition. This question can be addressed in future experiments by constructing concatemeric HCN channels (47, 48) with different subunits specifying a defined stoichiometry. Knowing these values it will become possible to analyze single native channels in neurons or SA node cells to learn to what extent these heteromers contribute to the pacemaker current in the physiological context.

Conclusions

Our analysis of single-channel currents in all four mammalian HCN channels demonstrates that the single-channel conductance is in the range of 1 pS, thereby, however, differing by a factor of up to 3 with $\gamma_{mHCN2} > \gamma_{mHCN1} > \gamma_{mHCN3}, \gamma_{mHCN4}, \gamma_{hHCN4}$. These differences in the conductance are not generated by the two narrow pore parts, the selectivity filter and the inner gate, but by four negative charges in the outer channel vestibule, leading there to an enrichment of the permeating K^+ ions. Coexpression of mHCN1, mHCN3, or mHCN4 with mHCN2 demonstrates conductance values in between those of the respective homomeric channels. Our approach provides insights into the function of homomeric and heteromeric HCN channels which has great potential for the development of highly specific drugs for the different isoforms and their heteromers.

Materials and Methods

Oocyte Preparation and cRNA Injection. Oocytes were surgically harvested under anesthesia (0.3% 3-aminobenzoic acid ethyl ester) from adult females of *Xenopus laevis*. The procedures regarding the *X. laevis* frogs were approved by the animal ethics committee of the Friedrich Schiller University Jena (UKJ-18-008 from 09 May 2018). The respective protocols were performed in accordance with the approved guidelines. Extreme efforts were made to reduce the stress and to keep the number of frogs to a minimum.

The oocytes were incubated with collagenase A (3 mg/mL, Roche, Grenzach-Wyhlen, Germany) for 105 min in Ca^{2+}-free Barth´s solution which contained (in mM) 82.5 NaCl, 2 KCl, 1 $MgCl_2$, and 5 HEPES, pH 7.5. Then, oocytes at stages IV and V were manually isolated. They were injected with about 50 ng of cRNA transcribed from the respective coding sequences in pGEM derivatives. We used WT mHCN1 (NM_010408), mHCN2 (NM_008226), mHCN3 (NM_008227), and mHCN4 (NM_001081192) as well as hHCN4 (NM_005477). After injection with cRNA, the oocytes were cultured at 18 °C in Barth solution containing (in mM) 84 NaCl, 1 KCl, 2.4 $NaHCO_3$, 0.82 $MgSO_4$, 0.41 $CaCl_2$, 0.33 Ca$(NO3)_2$, and 7.5 TRIS, pH 7.4. To gain reasonable expression for the different HCN isoforms, the incubation times were specific: mHCN1: 1 to 4 d, mHCN2: 1 to 4 d, mHCN3: 7 to 13 d, mHCN4: 3 to 9 d, hHCN4: 3 to 6 d.

Molecular Biology. The mouse HCN 1-4 and human HCN 4 genes and all modified subunits were subcloned behind the T7 promoter of pGEMHEnew. Point mutations and the pore exchange were introduced via the overlapping PCR-strategy followed by fragment subcloning using flanking restriction sites. Sequences were confirmed by restriction analysis and sequencing (Microsynth SEQLAB, Göttingen, Germany). cRNAs were prepared using the mMESSAGE mMACHINE T7 Kit (Thermo Fisher Scientific, Dreieich, Germany).

Two-Electrode Voltage Clamp. Currents in whole oocytes were recorded with the two-electrode voltage clamp (TEVC) technique (OC725C amplifier, Warner Instrument, Hampden, MA) at room temperature. Microelectrodes were filled with 3 M KCl. Their resistance was 0.3 to 1 MΩ. The experiments were conducted in ND96 medium containing (in mM) 96 NaCl, 10 HEPES, 2 KCl 1.8 $CaCl_2$, and 1 $MgCl_2$, pH 7.4. The medium was supplemented with 1 mM $BaCl_2$, 100 μM $LaCl_3$, and 100 μM $GdCl_3$ to minimize impact of endogenous channels (49). The experiments were controlled by the HEKA Patchmaster software (v2x90.5) and LIH8+8 hardware (HEKA Elektronik Dr. Schulze GmbH, Lambrecht, Germany). The holding potential was generally −30 mV. Ionic currents were measured with prepulses between −130 and −40 mV, spaced 10 mV, followed by a test pulse to −100 mV used to determine steady-state activation. Because the activation kinetics of mHCN1 is much faster than that of the other isoforms, the prepulse duration for mHCN1 was set to 1 s, whereas for the other channels, it was set to 4 s.

Steady-state activation was determined from the amplitude of the instantaneous current at the test pulse of −100 mV, measured as mean current of the time interval 5 to 10 ms (mHCN1) or 10 to 40 ms (other tested HCN isoforms) after the begin of the test pulse. The relative amplitude of the tail current, I/I_{max}, was determined by relating the actual amplitude I of the instantaneous current to I_{max} following the prepulse to −130 mV. This relationship was plotted as function of voltage and fitted by the Boltzmann function

$$\frac{I}{I_{max}} = \frac{1}{\left\{ 1 + exp\left[\frac{z\delta F(V - V_h)}{RT} \right] \right\}},$$ [1]

yielding the midpoint voltage V_h of half-maximum activation and the equivalent gating charge $z\delta$. R is the molar gas constant, T the temperature in Kelvin (K), and F the Faraday constant.

The activation speed was quantified by a time constant τ_{act} that was obtained by fitting the following function to the current time courses

$$I(t) = \begin{cases} I_{inst}, \text{ for } (t < t_0) \\ A \times \left\{ 1 - exp\left[-\frac{(t - t_0)}{\tau_{act}} \right] + I_{inst} \right\}, \text{ for } (t \geq t_0). \end{cases}$$ [2]

A and I_{inst} are the amplitude of the time-dependent and time-independent current (leak plus instantaneous current), respectively; t_0 is a delay interval.

Fits were performed by the nonlinear least-squares fitting routines implemented in the IgorPRO (Wavemetrics, Lake Oswege, OR) and OriginPro 2016G software (OriginLab Corporation, Northampton, MA).

Patch-Clamp Recording of Macroscopic mHCN3 Currents. For determining steady-state activation of mHCN3 channels with and without 20 μM cAMP, macroscopic currents were recorded from inside-out patches. The patches were positioned in front of solution outlets for either control bath solution without and with cAMP. The pipette resistance was 1.7 to 2.4 MΩ. The other recording conditions were similar to the single-channel recordings.

Steady-state activation was measured analog to the TEVC recordings by a double pulse protocol in which the hyperpolarizing pulses of 4 s duration were followed by a pulse to −100 mV. The normalized amplitude of the instantaneous current at −100 mV was plotted as function of voltage and fitted by Eq. **1**. Due to the exceptional low expression density, even after more than 7 d incubation time, it seemed that reasonable macroscopic recordings were only obtained from large patches which were presumably located in the pipette interior. This seemed to impede the effectiveness of the solution exchange which might have led to an underestimation of the cAMP-induced shift of V_h.

Patch-Clamp Recording at Single-Channel Resolution. Currents with single-channel resolution were recorded with the patch-clamp technique from either cell-attached or inside-out patches of *Xenopus* oocytes expressing the respective channels. The patch pipettes were pulled (P-2000 puller, Sutter Instruments, Novato, CA) from thick-walled quartz tubing (outer and inner diameter 1.0 and 0.5 mm, respectively) (Science Products GmbH, Hofheim, Germany) to keep the RC and dielectric noise as low as possible (50). The resistance of the pipettes was 7 to 20 MΩ. The bath and pipette solution contained (in mM) 100 KCl, 10 EGTA, 1 $MgCl_2$, 10 HEPES (pH 7.2) and 120 KCl, 10 HEPES, 1 $MgCl_2$, 1 $CaCl_2$ (pH 7.2) respectively. Mg^{2+} was added to elevate patch stability. In part of the experiments, cAMP (Sigma-Aldrich Corp., St. Louis, MO) was applied to the bath solution to reach, after gently stirring, the saturating concentration of 20 μM.

Particular care was taken to shield the measurements from external interfering: We followed the strategy to position an additional small Faraday box, surrounding the pipette and the bath, in the large Faraday box surrounding the microscope with the headstage (cage-in-cage strategy). With this shielding, we could reliably remove all 50 Hz components. Occasional spikes, presumably by inductive sources, could not be completely removed but were sufficiently rare to exclude these traces if required.

Currents were recorded at room temperature with an Axopatch 200B amplifier (Axon Instruments Inc., Foster City, CA). To minimize in inside-out patches effects of the rundown phenomenon typical for HCN channels (1, 2, 51), the measurements were started only 180 s after the patch excision. Stimulation and data recording were performed with the ISO3 hard- and software (MFK, Niedernhausen, Germany). The sampling rate was 20 kHz for the faster mHCN1 channels and 5 kHz for the other channels. The on-line filter of the amplifier (4-pole Bessel) was set to 1 kHz. The holding potential was generally −30 mV. The used voltages of the test pulses are indicated in the figures and the diagrams.

Hyperpolarizing pulses were sufficiently long to reach significant activation at the end of the pulses. For mHCN1, the pulse duration was 200 ms, for mHCN2 500 ms and for mHCN3, mHCN4 as well as hHCN4 4,000 ms. The respective intervals between the pulses were 200, 1,500, and 4,000 ms, respectively. It should be noted that for mHCN1 and mHCN2 the shorter pulses and higher repetition rates allowed us to get much larger numbers of traces than for the other slower channels. This provided the advantage to get empty traces (nulls) which could be subtracted from the individual traces with channel openings to perfectly abolish the capacitive artifacts. Reasonable patches had a seal resistance of >100 GΩ, in many cases 200 to 700 GΩ, or even higher. Such high values were a prerequisite to obtain sufficiently stable conditions for our analyses. These high resistances were not obtained with patches on HEK293 cells.

Single-Channel Analysis. The data of mHCN1 and mHCN2 were generally digitally filtered down to 200 Hz by the filter in the ISO3 software whereas those of mHCN3, mHCN4, and hHCN4 with smaller unitary currents were generally filtered down to 100 Hz. Filtering to the lower frequency of 50 Hz was only performed for

the analysis of unitary tail currents at −30 mV for HCN2 channels. The criterion for a channel opening was generally passing the 50% amplitude level.

For mHCN1 and mHCN2 channels, the short pulses provided sufficiently many empty traces without channel activity. These traces were averaged and subtracted from the traces with channel activity, providing the traces in Fig. 1 *A* and *B*, thereby taking advantage of the ISO3 analysis software to use a sliding null, i.e., five null traces as close as possible to the actual traces were formed and used. This resulted in an improved handling of subtle leak changes during the recording.

In case of the slower channels (mHCN3, mHCN4, hHCN4) the required usage of longer test pulses did not allow us to get as many traces as for the faster channels. We therefore determined the open probability from idealized traces.

To idealize raw traces, the difference between sliding averages preceding and following each current time point was calculated. Points within the expected rise-time, estimated as $(3f_c)^{-1}$, were omitted. The sliding average window was set to f_c^{-1}. Peaks in this difference trace were filtered for artifacts by enforcing minimum (typically 40 fA) and maximum amplitudes (typically 100 to 300 fA). All traces and gating events were screened and confirmed manually. Note that this strategy has a reduced sensitivity to detect events shorter than f_c^{-1}. The strategy was implemented in IgorPRO 7.0.8. (Wavemetrics, Lake Oswege, OR).

The channel number in a patch, *N*, was obtained from the highest number of unitary steps within a trace at −130 mV. The strategy was implemented in IgorPRO 7.0.8. (Wavemetrics, Lake Oswege, OR).

The amplitude of the unitary currents was determined locally by individual openings and closures. Because the open and closed times of the channels were reasonably long, it was easy to identify sufficiently many switch transitions from closed to open and open to closed, including also events for the opening of a second and a third channel if present. Such a switch transition contained at least 50 ms before and 50 ms after the switch event. For the analysis of patches with multiple coexpressed channels, also shorter time intervals before and after an opening transition of 15 ms were used. From these trace segments, an amplitude histogram was built and fitted by the sum of two, or sometimes three, Gaussian functions (Fig. 1 *C* and *D*). The chosen bin widths depended on the type of channel and were 12 to 20 fA. In case of the analysis of the unitary tail currents at −30 mV, filtered down to 50 Hz, the bin width was set exceptionally to 6 fA. The fits of the amplitude histograms were performed mainly with the implemented fit routine of the ISO3 software and in some cases also with the Origin Pro software (2019).

The single channel conductance *γ* of an individual opening was calculated by

$$\gamma = i/(V - V_{rev}), \quad \textbf{[3]}$$

where *i* is the unitary current obtained from a local amplitude histogram, *V* the actual voltage and V_{rev} the reversal potential set to 4.6 mV, according to the Nernst equation to

$$V_{rev} = -RT\ln(K_i/K_o) = -RT\ln(120 \text{ mM}/100 \text{ mM}) = 4.6 \text{ mV}, \quad \textbf{[4]}$$

with K_i and K_o being the K^+ concentrations in the bath and pipette solution. In cell-attached patches, the resting potential of the oocytes was assumed to be zeroed by the high K_o concentration in the bath.

Experimental data are given as mean ± SEM. Boxplots provide the mean (crosses), median (horizontal line), upper and lower quartiles (boxes), and maximum and minimum values (whiskers). Outliers are included.

In time courses of P_o, 95% CI (Fig. 1 *A–D* and *SI Appendix*, Fig. S3*A*) were estimated from summed idealized traces (52).

To enable inclusion of recordings in which clearly visible slow unitary HCN currents were superimposed by large needle-like spikes, presumably evoked by Ca^{2+}-activated chloride channels (53), we designed a selective median filter to eliminate these needle-like events. This filter was based on the difference between a median filtered (300 points) dataset and the raw data. Only for data points where this difference exceed a threshold, the raw values were replaced by values of the filtered trace. The replaced region was extended (3 to 13 points) to accommodate the filter frequencies used. *SI Appendix*, Fig. S9 illustrates the power of our median filter for a cell-attached patch containing five mHCN2 channels. In case that the median filter was used for displayed recordings, this is indicated in the figure legend. No amplitudes were analyzed on positions where data replacement took place.

Atomistic MD Simulation. The homology structure of different HCN channel variants (mHCN1, mHCN2, mHCN3, mHCN4, and hHCN4) was generated based on the cryo-EM structure of the open conformation of homotetrameric rabbit HCN4 channel [PDB ID: 7NP3, (23)]. This structure was selected due to its superior quality indicators and the inclusion of more refined loop regions compared to other deposited structures. For the preparation of the MD simulation setup, embedding of the entire HCN channels into a 1-palmitoyl-2-oleoyl-sn-glycero-3-phosphocholine (POPC) lipid membrane was carried out in CHARMM-GUI (54), where all endogenous ligands were removed before the simulations. All titratable residues of the protein were protonated according to their standard protonation state at pH 7. The simulations were performed with Amber19sb force field (55) using TIP3P water model (56). All the simulations were performed with GROMACS software package version 2023.3 (57) with 900 mM KCl. The system was first equilibrated in 6 steps using default scripts provided by the CHARMM-GUI webserver. A time step of 2 fs was used in the simulations of 1.875 ns for equilibration. We prepared two simulation setups. For mHCN1, mHCN2, mHCN3, mHCN4, and hHCN4 simulations, we conducted three independent runs of production simulations without transmembrane voltage, each 200 ns using an integration time step of 2 fs. Besides, we also conducted five independent simulation runs of mHCN2 with each 1,000 ns at 700 mV transmembrane voltage by using external electric field (58). All simulations' details are summarized in *SI Appendix*, Tables S4 and S5. Short-range electrostatic interactions were calculated with a cutoff of 1.0 nm, whereas the long-range electrostatic interactions were treated by the particle mesh Ewald method (59). The cutoff for van der Waals interaction was set to 1.0 nm. The simulations were performed at 300 K with an enhanced Berendsen thermostat [GROMACS V-rescale thermostat, (60)]. The Parrinello-Rahman barostat (61) was employed to keep the pressure within the system remaining at 1 bar.

All bonds were constrained with the Linear Constraint Solver (LINCS) algorithm (62). All trajectories were analyzed with GROMACS toolkits and Python3 using MDAnalysis (63). To calculate the residue-wise ion occupancy, we considered a residue to be interacting with an ion if the distance between them was less than the hydration radius of K^+, which is 3.4 Å. Molecular visualizations were made with PyMol and Visual MD (VMD) (64).

Data, Materials, and Software Availability. The input files of MD, comprising the starting configuration and all necessary parameters for performing the MD simulations, as well as structures of homology modeling are deposited in Zenodo (37). All other data are included in the Open Science Framework (65). All other data are included in the manuscript and/or *SI Appendix*.

Author affiliations: ªInstitut für Physiologie II, Universitätsklinikum Jena, Friedrich-Schiller-Universität Jena, Jena 07740, Germany; ᵇLeibniz-Forschungsinstitut für Molekulare Pharmakologie, Berlin 13125, Germany; and ᶜInstitute of Chemistry, Technical University of Berlin, Berlin 10623, Germany

1. D. DiFrancesco, Characterization of single pacemaker channels in cardiac sino-atrial node cells. *Nature* **324**, 470–473 (1986).
2. A. Ludwig, X. Zong, M. Jeglitsch, F. Hofmann, M. Biel, A family of hyperpolarization-activated mammalian cation channels. *Nature* **393**, 587–591 (1998).
3. H. F. Brown, D. DiFrancesco, S. J. Noble, How does adrenaline accelerate the heart? *Nature* **280**, 235–236 (1979).
4. M. Biel, C. Wahl-Schott, S. Michalakis, X. Zong, Hyperpolarization-activated cation channels: From genes to function. *Physiol. Rev.* **89**, 847–885 (2009).
5. D. DiFrancesco, The role of the funny current in pacemaker activity. *Circ. Res.* **106**, 434–446 (2010).
6. C. Wahl-Schott, M. Biel, HCN channels: Structure, cellular regulation and physiological function. *Cell Mol. Life Sci.* **66**, 470–494 (2009).
7. B. Santoro, G. R. Tibbs, The HCN gene family: Molecular basis of the hyperpolarization-activated pacemaker channels. *Ann. N. Y. Acad. Sci.* **868**, 741–764 (1999).
8. U. B. Kaupp, G. Seifert, Molecular diversity of pacemaker ion channels. *Annu. Rev. Physiol.* **63**, 235–257 (2001).
9. T. M. Ishii, M. Takano, H. Ohmori, Determinants of activation kinetics in mammalian hyperpolarization-activated cation channels. *J. Physiol.* **537**, 93–100 (2001).
10. B. Santoro *et al.*, Molecular and functional heterogeneity of hyperpolarization-activated pacemaker channels in the mouse CNS. *J. Neurosci.* **20**, 5264–5275 (2000).
11. J. Stieber, G. Stockl, S. Herrmann, B. Hassfurth, F. Hofmann, Functional expression of the human HCN3 channel. *J. Biol. Chem.* **280**, 34635–34643 (2005).
12. W. N. Zagotta *et al.*, Structural basis for modulation and agonist specificity of HCN pacemaker channels. *Nature* **425**, 200–205 (2003).
13. A. Ludwig *et al.*, Two pacemaker channels from human heart with profoundly different activation kinetics. *EMBO J.* **18**, 2323–2329 (1999). https://doi.org/10.1093/emboj/18.9.2323.
14. C. P. Alvarez-Baron, V. A. Klenchin, B. Chanda, Minimal molecular determinants of isoform-specific differences in efficacy in the HCN channel family. *J. Gen. Physiol.* **150**, 1203–1213 (2018).
15. P. Mistrik *et al.*, The murine HCN3 gene encodes a hyperpolarization-activated cation channel with slow kinetics and unique response to cyclic nucleotides. *J. Biol. Chem.* **280**, 27056–27061 (2005).
16. S. Chen, J. Wang, S. A. Siegelbaum, Properties of hyperpolarization-activated pacemaker current defined by coassembly of HCN1 and HCN2 subunits and basal modulation by cyclic nucleotide. *J. Gen. Physiol.* **117**, 491–503 (2001).
17. C. Ulens, J. Tytgat, Functional heteromerization of HCN1 and HCN2 pacemaker channels. *J. Biol. Chem.* **276**, 6069–6072 (2001).
18. C. Altomare *et al.*, Heteromeric HCN1-HCN4 channels: A comparison with native pacemaker channels from the rabbit sinoatrial node. *J. Physiol.* **549**, 347–359 (2003).
19. F. Er *et al.*, Dominant-negative suppression of HCN channels markedly reduces the native pacemaker current I(f) and undermines spontaneous beating of neonatal cardiomyocytes. *Circulation* **107**, 485–489 (2003).
20. B. Much *et al.*, Role of subunit heteromerization and N-linked glycosylation in the formation of functional hyperpolarization-activated cyclic nucleotide-gated channels. *J. Biol. Chem.* **278**, 43781–43786 (2003).
21. C. H. Lee, R. MacKinnon, Structures of the human HCN1 hyperpolarization-activated channel. *Cell* **168**, 111–120.e111 (2017).
22. C. H. Lee, R. MacKinnon, Voltage sensor movements during hyperpolarization in the HCN channel. *Cell* **179**, 1582–1589.e1587 (2019).
23. A. Saponaro *et al.*, Gating movements and ion permeation in HCN4 pacemaker channels. *Mol. Cell* **81**, 2929–2943.e2926 (2021).
24. B. Yu *et al.*, Cryo-EM Structure of human HCN3 channel and its regulation by cAMP. *J. Biol. Chem.* **300**, 107288 (2024), 10.1016/j.jbc.2024.107288.
25. V. Burtscher *et al.*, Structural basis for hyperpolarization-dependent opening of human HCN1 channel. *Nat. Commun.* **15**, 5216 (2024).
26. D. DiFrancesco, M. Mangoni, Modulation of single hyperpolarization-activated channels (I(f)) by cAMP in the rabbit sino-atrial node. *J. Physiol. Lond.* **474**, 473–482 (1994).
27. W. Shi *et al.*, Distribution and prevalence of hyperpolarization-activated cation channel (HCN) mRNA expression in cardiac tissues. *Circ. Res.* **85**, e1–e6 (1999).
28. J. P. Dekker, G. Yellen, Cooperative gating between single HCN pacemaker channels. *J. Gen. Physiol.* **128**, 561–567 (2006).
29. S. Thon, R. Schmauder, K. Benndorf, Elementary functional properties of single HCN2 channels. *Biophys. J.* **105**, 1581–1589 (2013).
30. M. H. Kole, S. Hallermann, G. J. Stuart, Single Ih channels in pyramidal neuron dendrites: Properties, distribution, and impact on action potential output. *J. Neurosci.* **26**, 1677–1687 (2006).
31. A. Camara-Checa *et al.*, A gain-of-function HCN4 mutant in the HCN domain is responsible for inappropriate sinus tachycardia in a Spanish family. *Proc. Natl. Acad. Sci. U.S.A.* **120**, e2305135120 (2023).
32. G. Michels *et al.*, Single-channel properties support a potential contribution of hyperpolarization-activated cyclic nucleotide-gated channels and If to cardiac arrhythmias. *Circulation* **111**, 399–404 (2005).
33. T. A. Simeone, J. M. Rho, T. Z. Baram, Single channel properties of hyperpolarization-activated cation currents in acutely dissociated rat hippocampal neurones. *J. Physiol.* **568**, 371–380 (2005).
34. K. Benndorf, D. DiFrancesco, Missing validation of key features in HCN single-channel recordings. *Proc. Natl. Acad. Sci. U.S.A.* **121**, e2400523121 (2024).
35. J. Kusch *et al.*, Interdependence of receptor activation and ligand binding in HCN2 pacemaker channels. *Neuron* **67**, 75–85 (2010).
36. N. L. Wicks, K. S. Chan, Z. Madden, B. Santoro, E. C. Young, Sensitivity of HCN channel deactivation to cAMP is amplified by an S4 mutation combined with activation mode shift. *Pflugers Arch.* **458**, 877–889 (2009).
37. H. Liu, H. Sun, MD Source Data for "Subunit-specific conductance of single HCN pacemaker channels at femtosiemens resolution." Zenodo. https://zenodo.org/records/14278606. Deposited 4 December 2024.
38. J. H. Krumbach *et al.*, Alkali metal cations modulate the geometry of different binding sites in HCN4 selectivity filter for permeation or block. *J. Gen. Physiol.* **155**, e202313364 (2023).
39. A. Elbahnsi *et al.*, Interplay between VSD, pore, and membrane lipids in electromechanical coupling in HCN channels. *eLife* **12**, e80303 (2023).
40. D. A. Kopfer *et al.*, Ion permeation in K(+) channels occurs by direct Coulomb knock-on. *Science* **346**, 352–355 (2014).
41. W. Kopec *et al.*, Direct knock-on of desolvated ions governs strict ion selectivity in K(+) channels. *Nat. Chem.* **10**, 813–820 (2018).
42. J. P. Dekker, A. Fodor, R. W. Aldrich, G. Yellen, A perturbation-based method for calculating explicit likelihood of evolutionary co-variance in multiple sequence alignments. *Bioinformatics* **20**, 1565–1572 (2004).
43. H. Terlau *et al.*, Mapping the site of block by tetrodotoxin and saxitoxin of sodium channel II. *FEBS Lett.* **293**, 93–96 (1991).
44. N. Chiamvimonvat, M. T. Perez-Garcia, G. F. Tomaselli, E. Marban, Control of ion flux and selectivity by negatively charged residues in the outer mouth of rat sodium channels. *J. Physiol.* **491**, 51–59 (1996).

45. S. Mahdavi, S. Kuyucak, Mechanism of ion permeation in mammalian voltage-gated sodium channels. *PLoS ONE* **10**, e0133000 (2015).

46. Z. Chen *et al.*, EMC chaperone-Ca(V) structure reveals an ion channel assembly intermediate. *Nature* **619**, 410–419 (2023).

47. M. R. Sunkara, T. Schwabe, G. Ehrlich, J. Kusch, K. Benndorf, All four subunits of HCN2 channels contribute to the activation gating in an additive but intricate manner. *J. Gen. Physiol.* **150**, 1261–1271 (2018).

48. C. Ulens, S. A. Siegelbaum, Regulation of hyperpolarization-activated HCN channels by cAMP through a gating switch in binding domain symmetry. *Neuron* **40**, 959–970 (2003).

49. S. Vemana, S. Pandey, H. P. Larsson, Intracellular Mg^{2+} is a voltage-dependent pore blocker of HCN channels. *Am. J. Physiol. Cell Physiol.* **295**, C557–565 (2008).

50. K. Benndorf, "Low noise recording" in *Single-Channel Recording*, B. Sakmann, E. Neher, Eds. (Springer, ed. 2, 1995), pp. 129–146.

51. P. Bois, B. Renaudon, M. Baruscotti, J. Lenfant, D. DiFrancesco, Activation of f-channels by cAMP analogues in macropatches from rabbit sino-atrial node myocytes. *J. Physiol.* **501**, 565–571 (1997).

52. C. J. Clopper, E. S. Pearson, The use of confidence or fiducial limits illustrted in the case of the binomial. *Biometrika* **26**, 404–413 (1934).

53. W. M. Weber, Endogenous ion channels in oocytes of *Xenopus laevis*: Recent developments. *J. Membr. Biol.* **170**, 1–12 (1999).

54. S. Jo, T. Kim, V. G. Iyer, W. Im, CHARMM-GUI: A web-based graphical user interface for CHARMM. *J. Comput. Chem.* **29**, 1859–1865 (2008).

55. C. Tian *et al.*, ff19SB: Amino-acid-specific protein backbone parameters trained against quantum mechanics energy surfaces in solution. *J. Chem. Theory Comput.* **16**, 528–552 (2020).

56. W. L. Jorgensen, J. Chandrasekhar, J. D. Madura, R. W. Impey, M. L. Klein, Comparison of simple potential functions for simulating liquid water. *J. Chem. Phys.* **79**, 926–935 (1983).

57. M. J. Abraham *et al.*, GROMACS: High performance molecular simulations through multi-level parallelism from laptops to supercomputers. *SoftwareX* **1–2**, 19–25 (2015).

58. C. Caleman, D. van der Spoel, Picosecond melting of ice by an infrared laser pulse: A simulation study. *Angew. Chem. Int. Ed. Engl.* **47**, 1417–1420 (2008).

59. T. Darden, D. York, L. Pedersen, Particle mesh Ewald: An N·log(N) method for Ewald sums in large systems. *J. Chem. Phys.* **98**, 10089–10092 (1993).

60. G. Bussi, D. Donadio, M. Parrinello, Canonical sampling through velocity rescaling. *J. Chem. Phys.* **126**, 014101 (2007).

61. M. Parrinello, A. Rahman, Polymorphic transitions in single crystals: A new molecular dynamics method. *J. Appl. Phys.* **52**, 7182–7190 (1981).

62. B. Hess, H. Bekker, H. J. C. Berendsen, J. G. E. M. Fraaije, LINCS: A linear constraint solver for molecular simulations. *J. Comput. Chem.* **18**, 1463–1472 (1997).

63. N. Michaud-Agrawal, E. J. Denning, T. B. Woolf, O. Beckstein, MDAnalysis: A toolkit for the analysis of molecular dynamics simulations. *J. Comput. Chem.* **32**, 2319–2327 (2011).

64. W. Humphrey, A. Dalke, K. Schulten, VMD: Visual molecular dynamics. *J. Mol. Graph.* **14**, 27–38 (1996).

65. K. Benndorf, Subunit-specific conductance of single homomeric and heteromeric HCN pacemaker channels at femtosiemens resolution. OSF. https://osf.io/q4e5d/. Deposited 6 December 2024.